Variations in mid-ocean ridge CO_2 emissions driven by glacial cycles

CrossMark

Jonathan M.A. Burley [*], Richard F. Katz

Department of Earth Sciences, University of Oxford, UK

A B S T R A C T

The geological record documents links between glacial cycles and volcanic productivity, both subaerially and, tentatively, at mid-ocean ridges. Sea-level-driven pressure changes could also affect chemical properties of mid-ocean ridge volcanism. We consider how changing sea-level could alter the CO_2 emissions rate from mid-ocean ridges on both the segment and global scale. We develop a simplified transport model for a highly incompatible trace element moving through a homogeneous mantle; variations in the concentration and the emission rate of the element are the result of changes in the depth of first silicate melting. The model predicts an average global mid-ocean ridge CO_2 emissions rate of 53 Mt/yr or 91 Mt/yr for an average source mantle CO_2 concentration of 125 or 215 ppm by weight, in line with other estimates. We show that falling sea level would cause an increase in ridge CO_2 emissions about 100 kyrs after the causative sea level change. The lag and amplitude of the response are sensitive to mantle permeability and plate spreading rate. For a reconstructed sea-level time series of the past million years, we predict variations of up to 12% in global mid-ocean ridge CO_2 emissions.

© 2015 The Authors. Published by Elsevier B.V. This is an open access article under the CC BY license (http://creativecommons.org/licenses/by/4.0/).

1. Introduction

Glacial cycles transfer $\sim 5 \times 10^{19}$ kg of water between the oceans and ice sheets (Tushingham and Peltier, 1991), leading to accumulation and ablation of kilometres of ice on the continents and sea-level change of $\sim$100 m. In Iceland, for example, the pressure change associated with melting of the ice sheet since the last glacial maximum had well-documented consequences for the volcanic activity (Sigvaldason et al., 1992; Jull and McKenzie, 1996; Maclennan et al., 2002) and lava geochemistry (Maclennan et al., 2002). More broadly, continental volcanism in both the northern and southern hemispheres shows increased activity associated with the last deglaciation (Gardeweg et al., 1998; Jellinek et al., 2004; Huybers and Langmuir, 2009). Huybers and Langmuir (2009) and Lund and Asimow (2011) hypothesised that the pressure variations caused by changing sea level during glacial cycles would affect mid-ocean ridge (MOR) volcanism. Crowley et al. (2015) documented variations of bathymetry near the Australian–Antarctic ridge that are possible evidence of such glacial effects.

A simple argument shows that variations in crustal thickness and sea-floor relief should be expected to result from sea-level variation. The melting rate of a parcel of mantle beneath a MOR is proportional to its depressurisation rate. As the parcel upwells, it depressurises due to the decreasing height of rock above it. The rate of change of pressure due to upwelling is the gravitational acceleration g times the mantle density times the upwelling rate ($\sim$3 cm/yr). Sea-level variation can modify this depressurisation rate: the pressure change due to varying sea level is the product of g, water density and the rate of change of sea level (up to 100 m in 10 kyr or 1 cm/yr). Water is about one third the density of the mantle and sea-level changes can be equivalent to one third the mantle upwelling rate, implying that sea-level changes can modify depressurisation rates, and hence melting rates, by up to $\pm$10%. Crowley et al. (2015) apply a paleo-sea-level reconstruction to a simulation of MOR melting and melt transport, with melting rates varying according to the variable pressure exerted by sea level. This leads to varying melt flux at the ridge, predicting variations in crustal thickness consistent with bathymetric observations of sea-floor relief.

Given this evidence for glacial cycles affecting MOR melt production, it is reasonable to consider if, as in Iceland (Maclennan et al., 2002), the chemistry of the lavas is also affected. To investigate this we develop a model of the transport of a highly incompatible element from the asthenosphere through the melting region to the MOR. Highly incompatible elements partition strongly into the melt, rather than remaining in the residual solid. Approximating this as complete incompatibility creates useful simplifications in modelling. For instance, a completely incompatible element's path through the melting region is entirely determined by the motion of the melt, without any need to consider that element in the solid or partitioning between phases. Furthermore, for small perturbations to the melting rate (such as those caused by sea-level change) the

* Corresponding author.
E-mail address: jonathan.burley@earth.ox.ac.uk (J.M.A. Burley).

mass-flow rate of the element through the MOR is constant (see Appendix A.4).

In a simple model of melting beneath a mid-ocean ridge, a parcel of mantle upwells adiabatically beneath the ridge axis, cooling slightly due to its expansion. The pressure-dependent solidus temperature of that parcel decreases as it ascends; at some depth (or, equivalently, pressure), the temperature of the parcel is equal to its solidus temperature. This depth, thought to be around 60 km, is called the depth of first silicate melting. With further upwelling, the parcel's temperature exceeds the solidus and it partially melts. As soon as the first increment of melt is produced, 100% of the completely incompatible element that was locally present in the solid mantle is transferred to the melt. Because the mantle is permeable and the melt is less dense than the residue, the melt ascends faster than the solid, segregating from its source. Melt segregation and transport of incompatible elements thus begins at a pressure-dependent depth. More specifically, melt segregation begins at a fixed pressure, but the depth corresponding to this pressure can change. We assume that there is no isostatic rebound associated with sea-level change and hence mantle upwelling is constant. Variations in sea level will therefore cause the depth of first silicate melting (and initiation of melt segregation) to rise and fall. The rate at which mantle crosses this boundary and delivers its content of incompatible elements to the melting region is the mantle upwelling rate minus the rate of upward motion of the boundary. So in this model, variations in the depth of first silicate melting cause variations in the flux of an incompatible element. As sea level falls, the depth of first melting increases, upwelling mantle crosses into the melting region faster, and the flux of incompatible element increases; the reverse is true for sea-level rise. Any perturbation to the melting rate within the melting region does not alter the mass of the incompatible element in the melt, it only dilutes (or concentrates) the element. Variations in melt-transport rate associated with melting perturbations are a secondary effect and are not considered in detail here (though see Appendix A.4).

A more nuanced view of melting may disagree with this simple story in some of the details, especially with the inclusion of volatile elements that are present in small concentrations in the mantle. Experimental evidence suggests that CO_2-rich melt forms at ∼250 km depth (Dasgupta et al., 2013) and has a low viscosity that rises sharply with silica content at shallower depth (Kono et al., 2014). If such carbon-rich melts can segregate from the solid mantle it would complicate the role of the transition to silicate melting at around 60 km. However, it remains an open question whether oxygen fugacity allows such melts to form and, if they do form, whether such tiny melt fractions can segregate from the solid mantle. Dasgupta et al. (2013) suggests carbonatite melt fractions reach ∼0.03 wt% deep in the mantle below ridges, which is at the lowest limit of carbonatite melt interconnectivity of 0.03–0.07 wt% in ∼0.05 mm olivine grains (Minarik and Watson, 1995). The additional presence of water might increase the melt fraction to 0.06–0.1 wt% (Dasgupta et al., 2013) by 150 km depth, but the threshold for interconnectivity of such melts is not known. In our calculations, we assume that these melt fractions do not segregate from the solid mantle until the onset of volatile-free peridotite melting at ∼60 km raises the melt fraction, creating an interconnected, permeable network of pores.

Among the highly incompatible elements, we focus on carbon despite its active role in the thermodynamics of melt production because variations in CO_2 emissions from the solid Earth are potentially important to understanding past variation of the climate. The solid Earth contains 10^{10}–10^{11} Mt carbon (Dasgupta and Hirschmann, 2010), orders of magnitude more than the atmosphere (0.6×10^6 MtC; Solomon et al., 2007) and the oceans (4×10^7 MtC; Solomon et al., 2007). Solid-Earth carbon emissions

from MORs are estimated as ∼25 MtC/yr (Coltice et al., 2004; Cartigny et al., 2008; Marty and Tolstikhin, 1998) and from arc volcanoes ∼20 MtC/yr (Coltice et al., 2004). As the largest reservoir, the solid Earth's carbon budget is known to control atmospheric carbon on multi-Myr timescales; geological ages show a correlation between volcanic activity and atmospheric CO_2 concentration (Budyko et al., 1987). Hence there is evidence for both MOR volcanism being affected by glacial cycles and for the effect of volcanic CO_2 emissions on atmospheric CO_2 concentration. While we focus on CO_2 in our model, the same theory applies equally to other highly incompatible elements such as U, Th, Nb, Ba, and Rb.

The model is developed under the guiding principle that it should be simple enough that the connections between the assumptions and the outputs are readily traceable. The full model is assembled from independent, decoupled parts that capture the key physics with minimal complexity. Mantle flow is modelled by the passively-driven corner-flow solution (Batchelor, 1967; Spiegelman and McKenzie, 1987); lithospheric temperature structure and thickness is computed with a half-space cooling model (Turcotte and Schubert, 2002). To quantify melt generation and transport we use one-dimensional compaction columns (Ribe, 1985; Hewitt, 2010) that are based on conservation of energy, mass, and momentum at steady state in a homogeneous mantle. The outline of the melting region is given by a parameterised solidus (Katz, 2008). A focusing width is applied such that melt focused to the ridge produces a maximum crustal thickness of 7 km. A detailed discussion of the assumptions made in deriving the model is presented below.

To summarise the results, the model predicts that a section of MOR spreading at 3 cm/yr half-rate will see a change in the rate of efflux of highly incompatible elements (e.g., CO_2) of ∼8% for a linear sea-level change of 100 m in 10 kyrs. For reconstructed sea level data and the present distribution of plate spreading rates, the model predicts global MOR emissions to deviate from the mean by up to ±6%. These results are sensitive to the permeability of the mantle, which is a primary control on the rate of melt transport. There are good constraints on how permeability scales with porosity, but its absolute value at a reference porosity (1% here) is uncertain. We consider a broad range of values that includes the most extreme estimates.

Section 2 details the model used to predict CO_2 emissions for a section of mid-ocean ridge; parameter values are stated in Table 1. The behaviour of the model is demonstrated for simple scenarios of sea-level variation in Sections 3.1–3.3; the model is applied to the global MOR system under a reconstructed sea-level history in Sections 3.4 and 3.5. The results are discussed in Section 4 and the key conclusions stated in Section 5.

2. The model

Our goal is to develop a method to compute the CO_2 emission rate E_{CO_2} (mass per unit time per unit length of ridge) from a segment of ridge. To achieve this we require a model of CO_2 flux into the melting region and also of its transport to the ridge. We approximate the behaviour of CO_2 as perfectly incompatible, and hence there is no exchange of CO_2 between phases during melt transport. The rate of ridge emission of CO_2 can then be quantified by integrating the mass flux into the base of the melting region f_{CO_2} (mass/area/time) and using the travel time from the base of the melting region to the ridge. This is formulated as

$$E_{CO_2}(t) = 2 \int_0^{x_f} f_{CO_2}(t_s, x, U_0) \, dx, \tag{1}$$

where x is the horizontal distance from the ridge axis, x_f is the maximum distance over which melt is focused to the ridge axis, U_0

Table 1
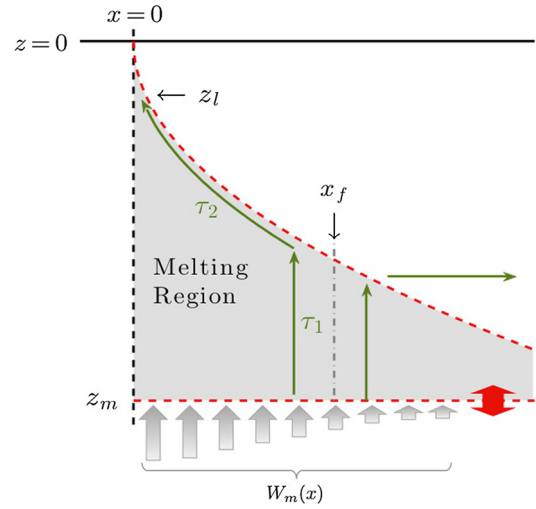Parameter values for calculations.

Parameter	Value		Parameter description
c	1200	J/kg/K	Specific heat
$\mathcal{C}_{CO_2}$	0.375	kg/m^3	CO_2 mass per m^3 of mantle (derived from 125 ppm by weight)
g	10	m/s^2	Gravitational acceleration
K_0	10^{-13}–10^{-11}	m^2	Permeability at 1% porosity
K	$K_0(\phi/\phi_0)^n$	m^2	Permeability
L	4×10^5	J/kg	Latent heat of the mantle
L_{MOR}	61 000	km	Total length of the mid-ocean ridge system
n	3	–	Porosity exponent in the permeability relation
S	[various]	m	Sea level, expressed as deviation from long term mean
$\dot{S}$	[various]	cm/yr	Rate of change of sea level with respect to time
$\widetilde{T}$	1648	K	Potential temperature of upwelling mantle
T_0	273	K	Ocean floor temperature
$T_{S_{ref}}$	1554	K	Reference solidus temperature
U_0	≤ 8	cm/yr	Plate half-spreading rate
x_f	10–70	km	Width of region, at z_m, from which melt is focused to the ridge
x_w	10–350	km	Width of melting region
z_m	60	km	Depth of first melting
α	3×10^{-5}	K^{-1}	Thermal expansion coefficient for the mantle
γ	60×10^{-9}	K/Pa	Clausius–Clapeyron slope of the mantle
η_f	1	Pa s	Mantle melt viscosity
κ	10^{-6}	m^2/s	Thermal diffusivity
Π	0.01	kg/m^4	Adiabatic melt productivity, kg of melt per m^3 of mantle per metre of upwelling
ρ	3300	kg/m^3	Mantle density
ρ_c	2900	kg/m^3	Oceanic crust (mean) density
ρ_w	1000	kg/m^3	Freshwater density
$\Delta\rho$	500	kg/m^3	Density difference between liquid and solid mantle
ϕ_0	0.01	–	Reference porosity (volume fraction)

Fig. 1. Sketch of the melting region. Two example melt streamlines are shown in green. Mantle upwelling rate into the base of the melting region W_m is represented by grey arrows, the size of which shows the decreasing magnitude of W_m with distance from the ridge axis. The red arrow indicates the variability of z_m with respect to time, expressed in equation (6) (all other boundaries are steady state). The melt streamlines on either side of the maximum focusing distance x_f show melt flow to the ridge or frozen into the lithosphere. (For interpretation of the references to colour in this figure legend, the reader is referred to the web version of this article.)

is the half-spreading rate, and t is time. A parcel of melt arriving at the ridge axis at time t was produced by mantle that crossed into the melting region at time t_s. The travel time of melt from the base of the melting region to the ridge is represented as τ, which varies with lateral distance x from the ridge axis. Hence the source time is $t_s(x) = t - \tau(x)$. The factor of two in eqn. (1) arises from the symmetry of the melting region across the ridge axis. A sketch of half the melting region is shown in Fig. 1.

Equation (1) requires an expression for f_{CO_2}. This is a product of the rate at which mantle material crosses the depth of first silicate melting z_m and the CO_2 concentration in that material. For generality, we consider an expression that allows for volatile-enriched incipient partial melting beneath the depth of first silicate melting, though we will later exclude this scenario from consideration. Thus, f_{CO_2} is written as

$$f_{CO_2}(t_s, x, U_0) = \left(W_m(x, U_0) - \frac{dz_m(t_s)}{dt} \right)(1 - \phi)\,\mathcal{C}_{CO_2}^{solid}$$
$$+ \left(w_m - \frac{dz_m(t_s)}{dt} \right)\phi\,\mathcal{C}_{CO_2}^{melt} , \qquad (2)$$

where $W_m(x, U_0)$ is the upwelling rate of the mantle, w_m is the upwelling rate of incipient melt, $\mathcal{C}_{CO_2}$ is a mass concentration of CO_2, and ϕ is the volume fraction of melt; all of these are evaluated at depth z_m and distance x from the ridge axis. The first term in parentheses on the right-hand side of the equation is the rate at which mantle crosses into the melting region. The concentrations and melt fraction may be considered steady-state, constant values as long as $w_m \geq W_m \geq \max(\dot{z}_m(t))$. This ensures that the

rate at which material crosses the depth of first silicate melting is always positive or zero. Even the fastest sea-level changes on record, meltwater pulses during the last deglaciation, satisfy these conditions for most MORs: 20 m sea level change in 500 yrs gives $\dot{z}_m = 1.3$ cm/yr. However, meltwater pulse events are not resolved in the reconstructed sea-level series that we consider in this paper (Siddall et al., 2010), so the conditions $w_m \geq W_m \geq \max(\dot{z}_m(t))$ are true with only occasional exceptions for the slowest spreading ridges. With these conditions satisfied and assuming that either $\phi(z_m) = 0$ or that $w_m = W_m$, equation (2) can be simplified to

$$f_{CO_2}(t_s, x, U_0) = \left(W_m(x, U_0) - \frac{dz_m(t_s)}{dt} \right)\mathcal{C}_{CO_2}. \qquad (3)$$

Here we should interpret $\mathcal{C}_{CO_2}$ as the mass concentration of CO_2 in the solid mantle plus co-moving incipient melt, if it is present. This model could be modified to accommodate more complicated situations, but this is not given further consideration at present.

The flux of CO_2 in equation (3) depends on the solid mantle upwelling rate at the depth of first silicate melting. Approximating this as passive (plate-driven) flow of isoviscous rock, mantle upwelling is given by the corner flow solution (Batchelor, 1967; Spiegelman and McKenzie, 1987). The vertical component of this solution, evaluated at $z = z_m$, can be written as

$$W_m(x, U_0) = \frac{2U_0}{\pi - 2\alpha_c - \sin 2\alpha_c} \left(\frac{1}{1 + \frac{x^2}{z_m^2}} - \sin^2(\alpha_c) \right), \qquad (4)$$

where the lithosphere is represented as a wedge with angle α_c to the horizontal. We follow Spiegelman and McKenzie (1987) in computing the wedge angle to approximately match the plate thickness at a specified distance from the axis. We use $\alpha_c = \tan^{-1}(z_l/x_w)$, such that the wedge intersects the upper boundary of the melting region z_l at the maximum width of melting region x_w (see Appendix A.3 for details). This definition of the wedge angle ensures that the lithospheric wedge does not overlap with the melting region, and that the upwelling rate is small but non-zero at the extreme width of the melting region ($0 \leq W_m(x_w) \ll U_0$).

An expression for the depth of first melting z_m is needed in equations (3) and (4). Taking decompression as the only influ-

ence on local mantle temperature prior to melting, we model the depth of first melting as the intersection between an adiabatic temperature profile and the solidus temperature profile. We approximate both profiles as linear with respect to depth (details in Appendix A.1) to obtain

$$z_m = -\left(\frac{\widetilde{T} - T_{S_{\mathrm{ref}}}}{\gamma \rho g - \frac{\alpha g \widetilde{T}}{c}}\right) + \frac{\rho_w}{\rho} S \ , \tag{5}$$

where $\widetilde{T}$ is the mantle potential temperature, $T_{S_{\mathrm{ref}}}$ is the solidus temperature at reference mantle composition and surface pressure, γ is the Clausius–Clapeyron slope for the mantle, ρ is the mantle density, α is the coefficient of thermal expansion, c is the specific heat capacity, S is the sea-level deviation from a long-term mean, and ρ_w is the density of water. The first term in equation (5) is the dry peridotite melting depth of ~60 km, and the second term is the shift in melting depth due to sea-level. The only time dependent variable in equation (5) is the sea level S, so differentiating gives

$$\frac{\mathrm{d}z_m}{\mathrm{d}t} = \frac{\rho_w}{\rho} \frac{\mathrm{d}S}{\mathrm{d}t}. \tag{6}$$

These equations state that silicate melting begins at a fixed pressure, but the depth corresponding to this pressure varies as sea level rises and falls.

The source time t_s used in equations (1) and (3) depends on the travel time of melt to the ridge from any point x along the base of the melting region. For simplicity, we consider melt flow as following a vertical path from the base to the top of the melting region, then following a high porosity channel along the impermeable top of the melting region to the ridge axis, as illustrated by streamlines τ_1 and τ_2 in Fig. 1. This is a reasonable approximation of numerically modelled streamlines for homogeneous mantle (*e.g.*, Katz, 2008), where buoyancy forces drive vertical fluid flow in the majority of the melting region, with the compaction pressure only becoming large enough to deflect melt flow from the vertical within a few kilometres of melt-impermeable boundaries (Sparks and Parmentier, 1991). We consider flow along the high porosity channel as instantaneous, motivated by the high flow rates expected there, as compared to vertical flow rates in the rest of the melting region (Katz, 2008). To compute the travel time from the base of the melting region to the base of the lithosphere, we use a 1D compaction column from Hewitt (2010). This model assumes Darcy flow and thermodynamic equilibrium for a two-component, homogeneous mantle with a constant Clausius–Clapeyron slope. Following the reduced model of Crowley et al. (2015), we assume that small variation in melting rates due to sea-level change do not significantly affect melt velocity or travel time. Furthermore, in computing τ we take z_m as constant, because changes in z_m due to sea level are only tens of metres, changing τ by $\ll 1\%$. This gives a travel time

$$\tau(W_m, z_l, z_m) = \phi_0 \left(\frac{\eta_f}{K_0 \Delta \rho g}\right)^{\frac{1}{n}} \left(\frac{\rho}{\Pi W_m}\right)^{1 - \frac{1}{n}} \left[n (z_l - z_m)^{\frac{1}{n}}\right] , \tag{7}$$

where η_f is the mantle melt viscosity, K_0 is the permeability of the mantle at the 1% reference porosity ϕ_0, $\Delta \rho$ is the density difference between the solid and melt, n is the porosity exponent in the permeability relation ($n \approx 2.7 \sim 3$, Miller et al., 2014), $z_l(x, U_0)$ is the depth of the upper boundary of the melting region, and Π is the adiabatic melt productivity (kg of melt produced per m^3 per m upwelling). This productivity is given by Hewitt (2010) as a ratio of thermodynamic parameters, and we retain the same parameter values here.

To close the model we need an expression for the upper boundary of the melting region $z_l(x)$. This boundary is located where the local temperature equals the solidus temperature, which is controlled by the thickness of the conductively cooled boundary layer that forms the lithosphere. Crowley et al. (2015) also included the effects of adiabatic decompression and latent heat removal, but this leads to an expression for $x_l(z)$ that cannot be inverted. However, as shown in Appendix A.2, the depth of this melting boundary is approximated by an isotherm of the half-space cooling model, which can be expressed as $z_l(x)$. This isotherm is hotter than the low-pressure solidus, but the temperature difference compensates for the change in solidus temperature with respect to depth. We use

$$z_l(x, U_0) = 2\sqrt{\frac{\kappa x}{U_0}} \ \mathrm{erfc}^{-1}\left(\frac{\widetilde{T} - T_l}{\widetilde{T} - T_0}\right) , \tag{8}$$

where T_l is the temperature of the upper boundary of melting region, assumed to be constant. T_0 is the temperature of the ocean floor, and κ is the thermal diffusivity of the mantle. Note that although we have neglected adiabatic decompression and latent heat of melting in equation (8), these are accounted for in the melting calculations.

3. Results

Below we demonstrate the behaviour of the model by a series of examples, then consider global CO_2 emissions for reconstructed sea level. We begin by modelling a unit length of mid-ocean ridge in the absence of sea-level change. This defines the baseline state of the model that we compare against when applying sea-level forcing. The first dynamic example is a single, linear sea-level change, which illustrates key characteristics of the model and emphasises the importance of the melt travel time. The emissions curve for this example approximates the Green's function for the model: the response to a step-change in sea level. We next consider simple, periodic sea level curves, demonstrating the system's response to an oscillatory forcing as a function of the frequency of that forcing. We then compute the model's response to a reconstructed Pleistocene sea-level record.

Building on these calculations for a single section of mid-ocean ridge, we calculate predictions for a global model, created by summing sections with appropriate spreading rates over the full MOR system. We demonstrate this composite model by considering the global emissions response to a single sea-level change and then to the reconstructed Pleistocene sea-level curve.

3.1. Constant sea level & baseline emissions

Baseline emissions are defined as the steady-state emission rate of CO_2 from the MOR for constant sea level. This represents the background state, which is disturbed after sea-level change. Fig. 2 shows baseline emissions as a function of plate spreading rate and demonstrates that, in the absence of changing sea level, CO_2 emissions per metre of ridge are approximately proportional to the half-spreading rate U_0. A faster spreading rate drives faster mantle upwelling, bringing more CO_2 into the melting region. Faster spreading rates also increase the width of the melting region (see Appendix A.3), leading to more melt and more CO_2 being focused to the ridge axis. However, not all melt produced is focused to the MOR; at some lateral distance, melts are frozen back into the lithosphere, rather than travelling to the ridge axis (e.g., Katz, 2008). We incorporate this detail by enforcing a maximum focusing width x_f such that melt focused to the MOR will produce crust ≤ 7 km thick in steady state, consistent with observations (White et al., 1992; Bown and White, 1994). Crustal thickness is calculated as the volume flow rate of melt to the ridge axis (kg m^{-3}
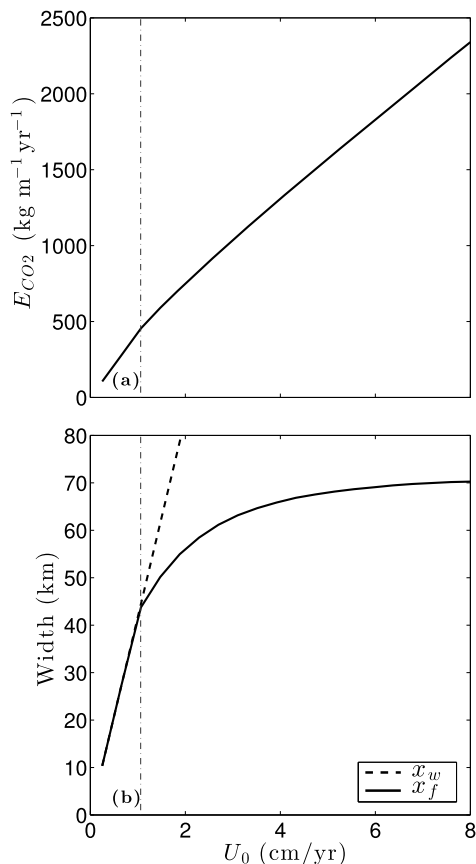
Fig. 2. (a) Ridge CO_2 emissions for constant sea level, and (b) focusing width x_f and full width x_w of the melting region; all shown for varying half-spreading rate. Focusing width is equal to the width of the melting region when crustal thickness is less than 7 km ($U_0 \leq 1$ cm/yr), and is otherwise limited such that crustal thickness does not exceed 7 km. The switch between these behaviours is marked by the grey dotted line at 1 cm/yr. E_{CO_2} is computed with CO_2 concentration in the mantle of 125 ppmw.

per metre along MOR axis) times the density ratio of basaltic melt to oceanic crust, divided by the half-spreading rate. At half-rates $U_0 \geq 1$ cm/yr, the focusing width is smaller than the width of the melting region. With the imposition of this limit on melt focusing, there is a slight change in the slope of the baseline emission curve at $U_0 = 1$ cm/yr (Fig. 2).

For the range of U_0 on Earth of up to 8 cm/yr, Fig. 2(a) shows baseline emissions of up to 2300 kg m^{-1} yr^{-1}. This is calculated using 0.38 kg CO_2 per m^3 of upwelling mantle (125 ppm CO_2 by weight, hereafter ppmw), based on an average of MOR source mantle of 50–200 ppmw (Dasgupta, 2013; Cartigny et al., 2008; Saal et al., 2002; Marty and Tolstikhin, 1998; Salters and Stracke, 2004). These source mantle CO_2 concentrations are inferred by four methods: *(i)* Cartigny et al. (2008) start with Nb concentration in MORBs, use Nb/C ratios, and assume an average degree of melting to calculate a CO_2 concentration in the source mantle. *(ii)* Saal et al. (2002) use MORB melt inclusions to measure CO_2 concentrations in the erupting mantle immediately prior to degassing, then assume an average degree of melting to calculate a CO_2 concentration in the source mantle. *(iii)* Marty and Tolstikhin (1998) use ^{3}He concentrations in the ocean to infer a ^{3}He efflux from MORs. Then they apply a He/C ratio to estimate carbon efflux from MORs, which is matched to a CO_2 concentration in the erupting mantle using a (completely degassed) crustal formation rate of 21 km^3/yr. CO_2 in the source mantle is then calculated by assuming an average degree of melting to generate MORB. *(iv)* Salters and Stracke (2004) start from major elements in the mantle and use a chain of

element ratios to derive a CO_2 concentration in the depleted mantle. For all these approaches, CO_2 concentration in the mantle is derived using several assumptions and has large uncertainties. The global MOR efflux of CO_2 is calculated using fewer assumptions and has less uncertainty. An alternative constraint on mantle CO_2 content is to match the global baseline emissions of the model to the estimated global MOR efflux by choosing a concentration of CO_2 in the source mantle of 215 ppmw (Section 3.5). This is effectively substituting our average degree of melting into other's calculations, and gives a result slightly higher than prior estimates of C_{CO_2}. For simplicity, we use a generally accepted 125 ppmw C_{CO_2} throughout this paper, but restate key results for the 215 ppmw value. This changes CO_2 emissions by a factor of 1.7, as emissions scale linearly with C_{CO_2} (see eqn. (3)).

Subsequent sections present scenarios of changing sea-level. In these sections, plots depict emissions in terms of percentage difference from baseline emissions for the appropriate half-spreading rate; these percentage values apply to all highly incompatible elements and for any C_{CO_2}. Percentage results can be converted to CO_2 mass via Fig. 2. The deviations from the baseline emission rate are a consequence of non-zero $\dot{z}_m$ in equation (3). By definition, total emissions are equal to this deviation summed with baseline emissions.

3.2. Single sudden change in sea level

Imposition of a sudden sea-level change exposes the behaviour of the model. We use a steep, linear ramp, which gives a box function in $\dot{S}$. Fig. 3 shows the predicted MOR CO_2 emission rate E_{CO_2} resulting from this sea level forcing. CO_2 emissions remain at the baseline level for ~90 kyrs after the change in sea level and then there is a sharp rise in E_{CO_2}, representing an 8% increase in emission rate. This delayed response is due to the travel time of CO_2 from the base of the melting region to the ridge. After the 8% peak, E_{CO_2} falls sharply to about 3%, followed by a slow decay until 130 kyrs, after which there is a linear drop back to the baseline level over the duration of the box-pulse in $\dot{S}$. The origin of this emissions pattern in Fig. 3(c) is explored in Fig. 4.

Fig. 4 demonstrates how the shape of the emission response curve in Fig. 3(c) is a consequence of the travel time τ and its variation with respect to distance x from the ridge axis. This travel time, shown in Fig. 4(c), ranges between $\tau_{\min}$ for melts originating in the mantle beneath the ridge axis and $\tau_{\max}$ for distal melts that are focused laterally. The mixture of melts that arrives at the ridge at time t contains CO_2 that was transported in melts that initiated along the base of the melting region at all $x < x_f$. These deep melts formed and began to segregate from their source at times in the past $t - \tau(x)$. The CO_2 content of the segregated melt is different to the baseline case according to the $\dot{S}$ value at $t - \tau(x)$. Therefore, we can calculate the deviation from the baseline by considering the rate of sea-level change (alternatively, $\dot{z}_m$) acting on the melting region when each element of melt first segregated. This is represented in Fig. 4(c), and the integral of this plot with respect to x is directly proportional to E_{CO_2} in Fig. 3.

The E_{CO_2} response is clarified by again considering a sharp, linear drop of sea level that occurs over the interval $0 \leq t \leq 10$ kyrs. The drop in sea level causes the depth of the base of the melting region to increase, importing additional CO_2 into the melting regime. In panels (a-i), (a-ii), and (a-iii) of Fig. 4 we see the box pulse receding into the past as time progresses over $t_1 < t_2 < t_3$ (Fig. 3c shows E_{CO_2} at these times). The start and end times of the pulse are projected onto $\tau(x)$ in panel (b). At t_1, the projection lines do not intersect $\tau(x)$, meaning that the CO_2 perturbation generated by $\dot{S}$ has not yet reached the ridge axis. Therefore the emissions curve in Fig. 3(c) remains at the baseline level. At t_2, the projection lines span $\tau_{\min}$; the shallow slope of $\tau(x)$ near $\tau_{\min}$
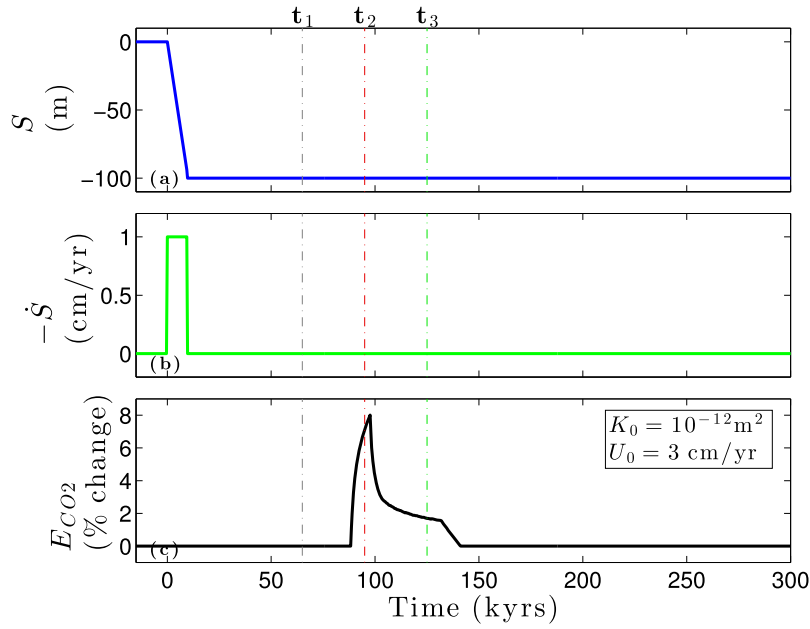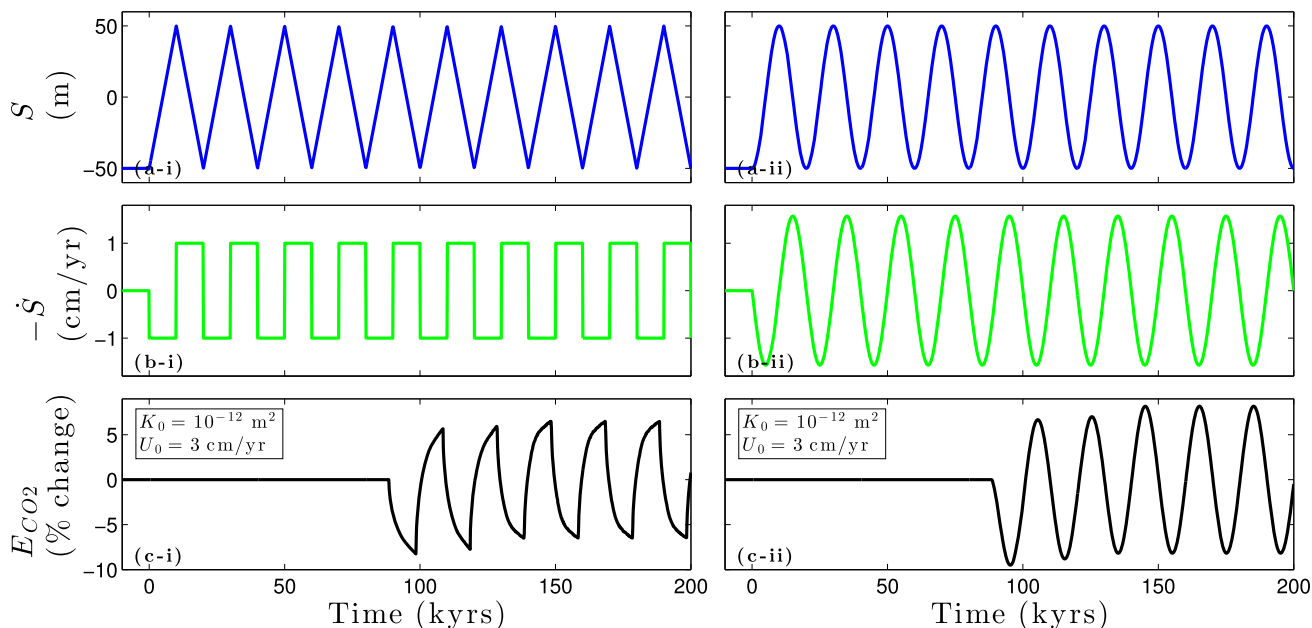
Fig. 3. Single step change in sea level. Plots show **(a)** sea-level change, **(b)** the negative rate of sea-level change, and **(c)** CO_2 emissions from a section of mid-ocean ridge, measured as percentage change from baseline emissions. The plate half-spreading rate and the permeability constant at 1% porosity are U_0 and K_0, respectively. The three times marked on the plots correspond to (a–i, ii, iii) in Fig. 4. Negative $\dot{S}$ is plotted so that peaks in $\dot{S}$ and consequent peaks in E_{CO_2} point in the same direction.
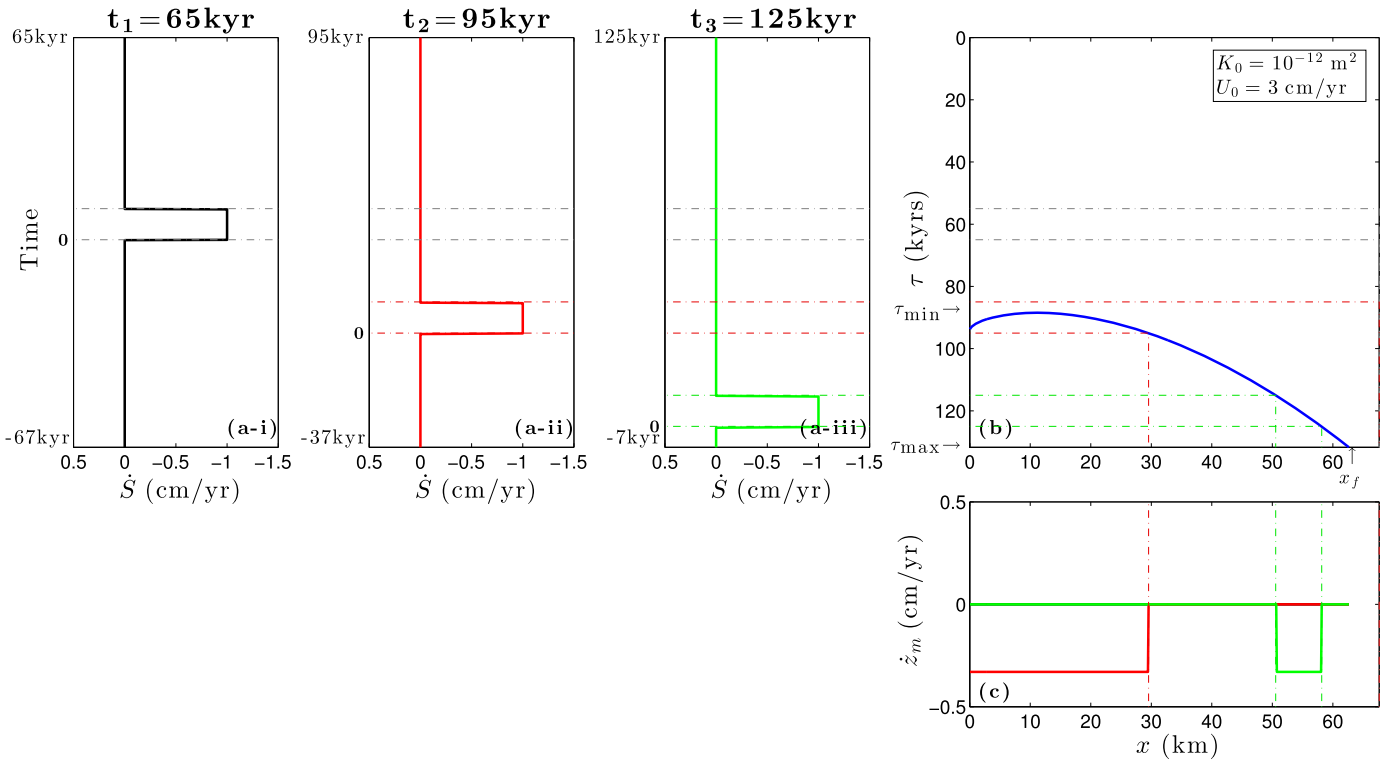
Fig. 4. The effect of a linear change in sea level on ridge CO_2 emissions. The three points in time shown in black, red, and green show the state of the system 65, 95, and 125 kyrs after the pulse began. Plots show: **(a–i, ii, iii)** rate of sea-level change from present into the past, for the three points in time marked in Fig. 3. **(b)** Travel time of melt from the base of the melting region to the ridge, increasing downwards. Travel time at $x = 0$ is slightly greater than τ_{min} because the sharp increase in lithospheric thickness within a few km of the ridge increases the column height; the effect of this increase in height exceeds the effect of faster on-axis upwelling. **(c)** Rate-of-change of the depth of first melting that acted on the melt currently arriving at the ridge axis, when that melt began to segregate. Dashed lines mark how the travel time converts $\dot{S}(t)$ to $\dot{z}_m(x)$. The integral of a coloured line from 0 to x_f in panel (c) is directly proportional to E_{CO_2} at the corresponding time in Fig. 3(c). This is expressed by the integral of $\dot{z}_m$ with respect to x in equation (3). A video animating this plot and E_{CO_2} over time is included in the online supplementary materials. (For interpretation of the references to colour in this figure legend, the reader is referred to the web version of this article.)

means that CO_2 from a broad (30 km) region affected by the $\dot{S}$ pulse is arriving at the ridge axis at t_2. This causes the spike in emissions shown in Fig. 3(c). At t_3, the interval of sea-level change has receded far into the past. The only CO_2 perturbation in melts

arriving at the ridge is in distal melts from the base of the melting region at 50 to 58 km off-axis. The narrowness of this band translates to a reduced (but non-zero) value of E_{CO_2} at t_3 in Fig. 3(c). As the sea-level drop recedes further into the past, the emission

Fig. 5. Sawtooth and sine waves in sea level starting at $t = 0$. Plots show **(a)** sea-level, **(b)** negative rate of sea-level change, **(c)** CO_2 emissions from a section of mid-ocean ridge. Considering the left column, each box-pulse in $\dot{S}$ produces an emissions peak/trough as in Fig. 3(c) with interference where they overlap, giving the net result seen in (c-i). The steady upward shift in the E_{CO_2}-peaks until ~150 kyr is due to this overlap. If the first box-pulse in $\dot{S}$ had been in the opposite direction, E_{CO_2} peaks in (c) would be mirrored across $E_{CO_2} = 0$.

rate drops to zero because the very distal melts (from $x > x_f$) are not focused to the ridge axis. This process is animated in a video in the online supplementary materials.

In the limit of vanishing duration of sea-level change, the pulse of $\dot{S}$ approximates to a Dirac delta function. Hence the E_{CO_2} response shown in Fig. 3(c) is an approximation of the Green's function. Conceptually, the emissions response for any sea-level time series could be approximated by convolution with a Green's function approximation like Fig. 3(c).

From this discussion, it is clear that changes to $\tau(x)$ will alter how MOR emissions respond to changing sea-level. Equation (7) for travel time shows that plate half-spreading rate U_0 and permeability constant K_0 are the key parameters affecting the melt travel-time τ. Higher values of either lead to shorter travel times, giving a higher peak in E_{CO_2} over a shorter time period, with this peak occurring sooner after the causative sea-level change. This is explored in more detail in the following section.

3.3. Oscillating sea level

We now consider oscillatory sea level and discuss the concepts of lag and admittance.

Fig. 5 shows a pair of oscillating sea level scenarios and their predicted E_{CO_2} variation. The left column (i) shows a time series of alternating box-pulses in $\dot{S}$; the right column (ii) shows a sinusoidal sea-level variation. Fig. 5(c-i) has an oscillating series of peaks in E_{CO_2} resulting from a series of $\dot{S}$ box-pulses in Fig. 5(b-i). This $\dot{S}$ series is equivalent to summing single box-pulses from Fig. 3(b), with suitable offset and amplitude. Similarly, the CO_2 emissions can be represented as a sum of offset emissions spikes from single, linear changes in sea level. The train of emissions peaks in Fig. 5(c-i) and (c-ii) stabilises in amplitude after $t \approx \tau_{max}$; this transient represents the spin-up time of the model, associated with the tail of excess emissions shown in Fig. 3.

Fig. 5(ii) shows sinusoidal sea level and provides the context to define the lag metric. Lag $\mathcal{L}$ is the time between a peak in $\dot{S}$ and the corresponding peak in emissions. Because the time interval around τ_{min} kyrs before t has the largest influence on E_{CO_2} at t, the E_{CO_2} signal should lag $\dot{S}$ by about τ_{min}. However, the lag

will not be exactly τ_{min}, as the influence of $\dot{S}$ on E_{CO_2} is felt up to τ_{max} years after the change in sea level. Thus the exact value of lag will be slightly greater than τ_{min} and we expect this difference to depend on the period of sea-level oscillation relative to $\tau_{max} - \tau_{min}$. In particular, when the period approaches and exceeds $2(\tau_{max} - \tau_{min})$, the lag becomes equal to the mean melt-transport time τ_{mean}. Fig. 6 shows lag, τ_{min}, τ_{mean}, and τ_{max} for varying half-spreading rate, permeability constant, and sinusoidal sea-level period. We note that $\tau_{min} \leq \mathcal{L} \leq \tau_{mean} \ll \tau_{max}$ and therefore we assume $\mathcal{L} \approx \tau_{min}$ with a small, systematic error.

Sinusoidal variation of sea level also provides a context in which compute admittance. Admittance is the ratio of the response amplitude to the forcing amplitude as a function of the sinusoidal forcing period. We define two versions of admittance: absolute admittance, with units of kilograms CO_2 per metre of ridge per year per 100 m of sea-level change, and relative admittance, with units of percentage change from baseline emission rate per 100 m of sea-level change. The latter is the absolute admittance divided by the baseline emission rate. Fig. 7 shows absolute and relative admittance and how they vary with changing sea-level period, half-spreading rate, and permeability constant. We discuss both the trends and the oscillations of these curves, starting with absolute admittance.

Absolute admittance (panels (a) and (b) of Fig. 7) depends on the period of sea-level oscillation, the permeability, and to a lesser extent, on the half-spreading rate. We consider these in turn. Shorter periods of sea-level variation at constant amplitude give larger values of $|\dot{S}|$ and $|\dot{z}_m|$, and hence increase the temporal variation of f_{CO_2}. This causes increased deviation of ridge emissions from baseline. Increased mantle permeability and spreading rate both reduce the melt travel-time from the base of the melting region. In the melt travel-time model of equation (7), the permeability appears as K_0, while the spreading rate U_0 is directly proportional to the mantle upwelling rate W_m. A reduced melt travel-time implies a smaller difference between τ_{max} and τ_{min}, and therefore a focusing of CO_2 from the base of the melting region to the ridge axis over a shorter interval in time. The uncertainty in mantle permeability translates to a broader spread of the
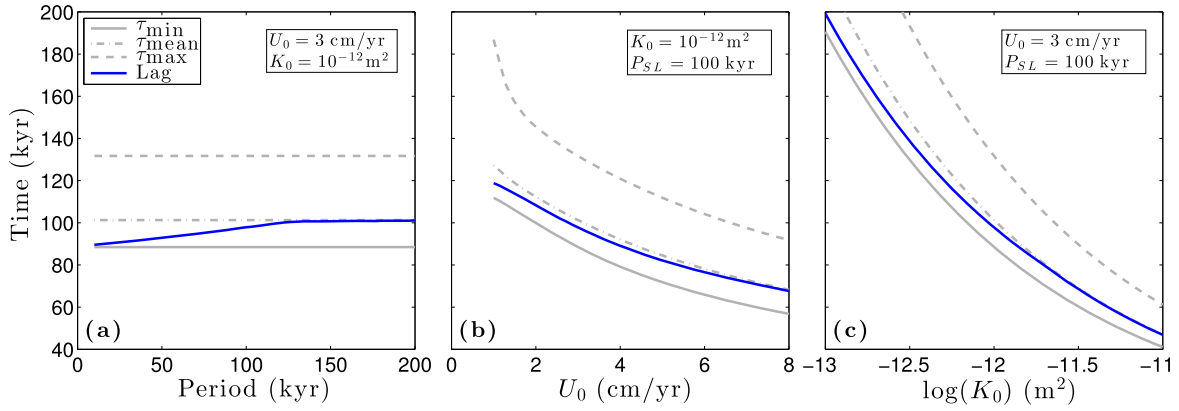
Fig. 6. Lag and travel time for varying **(a)** sinusoidal sea-level period, **(b)** half-spreading rate, and **(c)** permeability constant. The lag is calculated as the time between a peak in $-\dot{S}$ and the corresponding peak in E_{CO_2} for sinusoidal sea level.
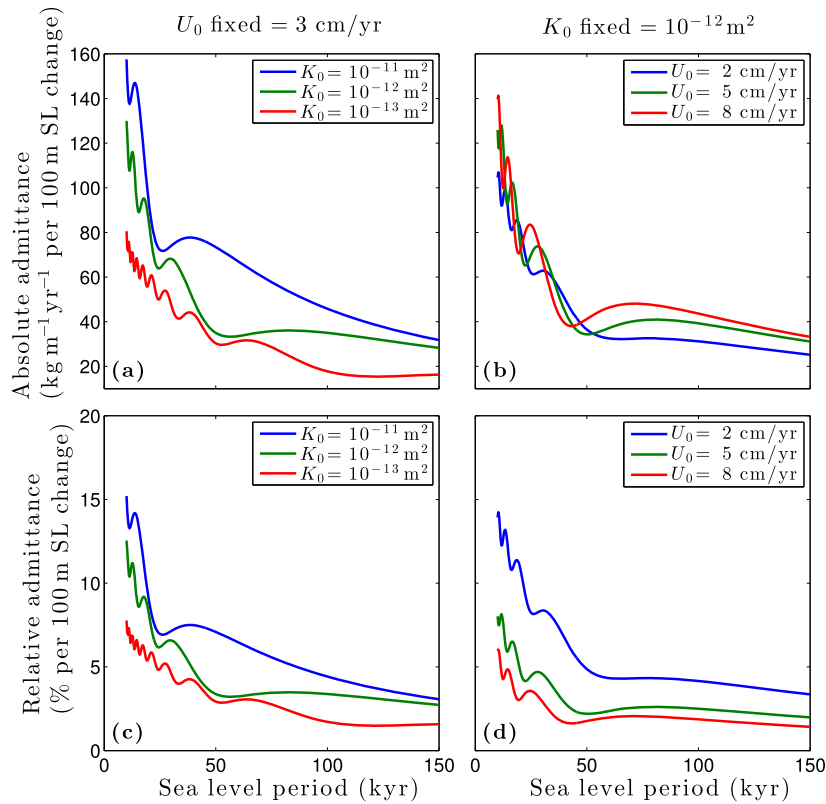
Fig. 7. Absolute and relative admittance for varying half-spreading rate, permeability, and sinusoidal sea-level period. Plots hold either U_0 or K_0 fixed. The magnitude of sea-level change is constant for all periods.

absolute admittance curves than does the range of half-spreading rates considered.

Relative admittance is equal to the absolute admittance normalised by the baseline emissions rate. The baseline depends on half-spreading rate but not on permeability (Fig. 2(a)). We therefore see a difference between absolute and relative admittance in Fig. 7(b) and (d). For slow-spreading ridges, which have a low baseline emissions rate, the normalised variance (and hence the relative admittance) is larger.

The oscillations superimposed on the primary admittance trend are not physically significant, but are readily explained. They arise from variation in the number of sea-level half-cycles that fit into the time interval from $t - \tau_{max}$ to $t - \tau_{min}$; this is the time interval over which $\dot{S}(t - \tau)$ can contribute CO_2 emissions at time t. For oscillatory sea level, each positive or negative peak in $\dot{S}$ has an

opposing emissions effect relative to the prior negative or positive peak. If there is an unmatched peak affecting the bottom of the melting region, the amplitude of E_{CO_2} variations is larger and the admittance is higher.

Broadly, the patterns of admittance and lag imply that, in terms of CO_2 emission variation, the dominant sea-level changes will be those with large amplitude and short period changes. The emissions variation associated with such changes will lag the forcing by approximately τ_{min}. The modelled magnitude and lag of E_{CO_2} changes are affected by both K_0 and U_0.

3.4. Reconstructed Pleistocene sea level

The simple scenarios of sea-level variation presented above give insight into the behaviour of the model, but are not representative
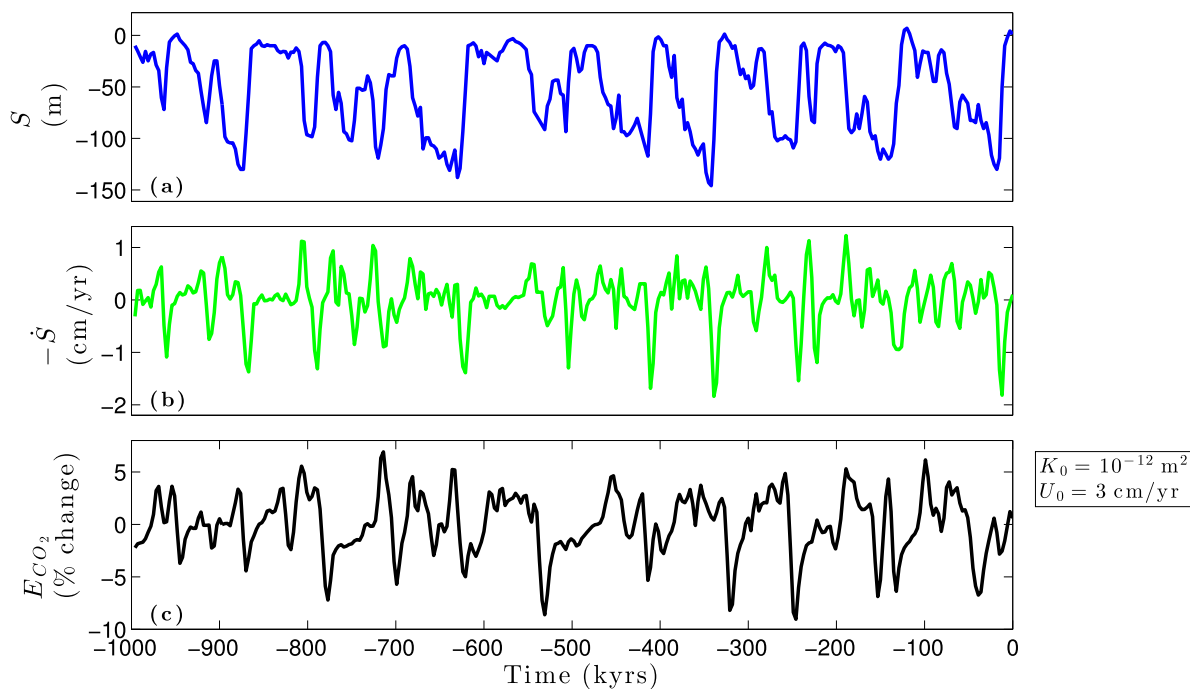
Fig. 8. Reconstructed sea level. Plots show **(a)** sea-level change, **(b)** the negative rate of sea-level change, and **(c)** CO_2 emissions from a section of mid-ocean ridge. The lag is ~90 kyrs.

of the variations that have occurred naturally, over the past million years. We move, therefore, to a model forced by the time-series of reconstructed global sea level from Siddall et al. (2010), shown in Fig. 8(a). Other reconstructions exist, but the differences between them are small enough that we follow Crowley et al. (2015) and consider only this one. Siddall et al. (2010) record data every 3 kyrs and, based on their reconstruction, the highest rates of sea-level change (Fig. 8(b)) meet the condition $\max(\dot{z}_m(t)) < W_m$ required for validity of equation (3).

Fig. 8(c) shows the result of applying reconstructed sea level to ridge E_{CO_2}. There is a $\pm 8\%$ range in E_{CO_2} for moderate half-spreading rate and permeability. The E_{CO_2} curve is, qualitatively, an offset version of $\dot{S}$ with small variations smoothed out — as expected from E_{CO_2} being approximated by convolving $\dot{S}$ with the emissions response in Fig. 3(c). Within this framework, we now consider how to apply the model to global MOR emissions.

3.5. Global mid-ocean ridges

The global MOR system is composed of ridge segments spreading at different rates, ranging from the ultra-slow Gakkel ridge to the fast East Pacific Rise. The baseline emissions depend on the half-spreading rate, as does the character of the emissions response to sea-level change. The global response to sea-level change should therefore be computed as the segment-scale response, integrated over the global MOR system,

$$\mathcal{G}_{CO_2}(t, K_0) = \int_0^{L_{MOR}} E_{CO_2}(t, K_0, U_0(l)) \mathrm{d}l, \qquad (9)$$

where $\mathcal{G}_{CO_2}$ is global MOR emissions of CO_2 in kg/yr, l is arc length along the ridge, and L_{MOR} is the total length of the MOR system. This integral can be approximated by discretising the half-spreading rate into bins U_{0i} and summing the local response in each bin. A weighting is applied to each entry in the sum to account for the total length of segments with half-spreading rates in that bin. The sum is written as

$$\mathcal{G}_{CO_2}(t, K_0) = \sum_{i=1}^{N} E_{CO_2}(t, K_0, U_{0i}) L_i(U_{0i}), \qquad (10)$$

where N is the total number of spreading rate intervals to sum over and $L_i(U_{0i})$ is the total length of MOR in a particular spreading-rate bin. The local emission rate E_{CO_2} in each bin is computed by adopting the average half-spreading rate of the bin and assuming that sea-level change is eustatic — the same for all segments globally.

Gale et al. (2013) provide a catalogue of segment lengths and spreading rates for the global MOR system; the total ridge length is 61 000 km with a mean half-spreading rate of 2.5 cm/yr. A histogram of these data is plotted in Fig. 9(a). Fig. 9(b) shows, for each spreading-rate bin, the rate of baseline emissions per metre of ridge. Panel (c) then shows the product of ridge length and emissions rate per metre, giving the total emissions rate associated with each spreading rate bin. These are summed in accordance with eqn. (10) to give the total baseline global response. The global baseline emission rate thus predicted is 53 Mt CO_2 per year assuming a sub-ridge mantle CO_2 concentration of 125 ppmw. This can be compared to other estimates of 91 ± 45 MtCO$_2$/yr (Coltice et al., 2004; Cartigny et al., 2008; Marty and Tolstikhin, 1998). If we instead constrain the model to have baseline emissions of 91 Mt CO_2/yr, it requires a sub-ridge mantle CO_2 concentration of 215 ppmw (0.65 kg per m^3).

Before applying the reconstructed sea-level forcing to the weighted global emissions sum in eqn. (10), we consider the simple sea level forcing that was used to probe the behaviour of E_{CO_2} in Fig. 3. This linear ramp in sea level is applied to compute the global emissions response in Fig. 10(a) for a range of mantle permeabilities. Global emissions in Fig. 10(a) are, unsurprisingly, more complex than the E_{CO_2} equivalent, as they consist of a summation of N E_{CO_2} peaks from Fig. 3, weighted according to the ridge length in each bin and offset due to the variation in τ with U_{0i}. Compared with Fig. 3, $\mathcal{G}_{CO_2}$ has a smaller percentage difference in the rate of CO_2 emissions and is spread out over a longer time-period.
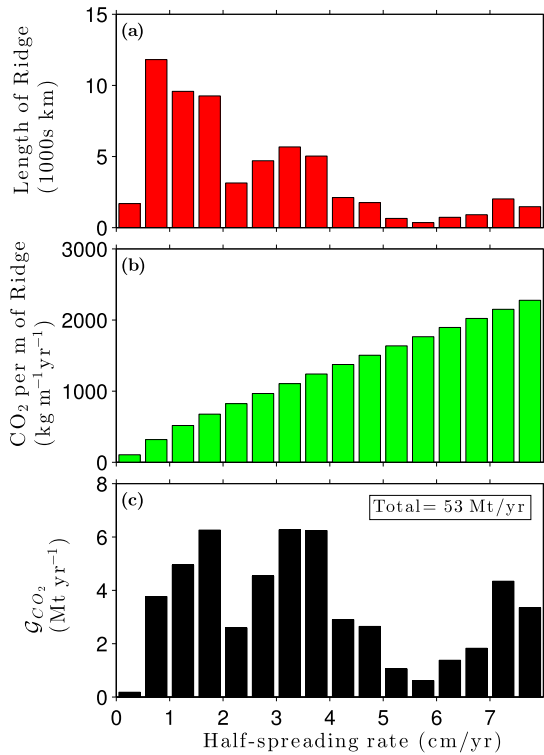
Fig. 9. Quantities associated with discrete bins of half-spreading rate. **(a)** The total length of MOR (Gale et al., 2013). **(b)** Baseline emissions per metre of MOR from our model. **(c)** Baseline global CO_2 emissions as the product of quantities in panels (a) and (b). Calculated for 0.38 kg CO_2 per m^3 of upwelling mantle (125 ppmw). Baseline emissions are independent of K_0.

Finally, we apply the reconstructed sea-level time series to the global model. Fig. 10 shows $\mathcal{G}_{CO_2}$ for reconstructed sea level, calculated and plotted for a set of three values of permeability constant K_0 in panels (d-i), (d-ii), and (d-iii). These curves demonstrate a reduction in $\mathcal{G}_{CO_2}$ range from 6.6 $MtCO_2$/yr for $K_0 = 10^{-11}$ m^2 to 1.2 $MtCO_2$/yr for $K_0 = 10^{-13}$ m^2. The reduction in $\mathcal{G}_{CO_2}$ range occurs because K_0 affects the range of τ_{min} that is implicit in the global sum in eqn. (10). A large value of K_0 gives higher overall permeability, shorter melt-transport times, and a global range in τ_{min} that is smaller. Therefore the emissions response to a box-pulse in $\dot{S}$ (Fig. 10(a)) is temporally concentrated and attains a higher peak value. Hence, larger K_0 causes greater amplitude of variation in $\mathcal{G}_{CO_2}$ for reconstructed sea level.

4. Discussion

The model prediction for global MOR CO_2 emissions at constant sea level using a mantle CO_2 concentration of 125 ppmw is 53 Mt CO_2 per year (14 Mt carbon per year), a value that is within error of estimates from analyses of mid-ocean ridge basalts of 91 ± 45 $MtCO_2$/yr (Coltice et al., 2004; Cartigny et al., 2008; Marty and Tolstikhin, 1998). However, note that our prediction is not independent of MORB studies because our choice of $\mathcal{C}_{CO_2}$ is based on observed MORB chemistry. If we instead choose to constrain the model to fit published CO_2 emissions, we require a source mantle CO_2 concentration of $\sim$215 ppmw.

The ranges in global CO_2 emissions under reconstructed variation of past sea level (Fig. 10 for 125 ppmw CO_2) are 1 $MtCO_2$/yr, 3 $MtCO_2$/yr, and 7 $MtCO_2$/yr for mantle permeabilities at 1% porosity of 10^{-13} m^2, 10^{-12} m^2, and 10^{-11} m^2 respectively. These idealised predictions assume that 100% of CO_2 transported to the ridge axis is degassed into the oceans, rather than retained in the crust or mantle. This may, in fact, be rather accurate; Cartigny

et al. (2008) estimated that over 80% of CO_2 in primitive MORB is degassed near the ridge axis. Furthermore, 100% degassing is assumed in the papers that calculate the source mantle CO_2 concentration we use. It has previously been speculated that variations in ridge CO_2 emissions would have an effect on global climate (Huybers and Langmuir, 2009; Lund and Asimow, 2011); it is beyond the scope of the present manuscript to investigate this question, though it is a target for future work.

Uncertainty in mantle permeability translates to uncertainty in both the amplitude of variations and the lag of global CO_2 emissions from MORs. There are various experimental constraints on mantle permeability (*e.g.* Miller et al., 2014; Connolly et al., 2009); these tend to agree on the scaling with porosity, but disagree on the magnitude of K_0. Furthermore, permeability is sensitive to grain size, a parameter that is poorly known for the mantle beneath MORs (although see Turner et al., 2015). Our chosen range of K_0 is intended to accommodate these uncertainties, as well as represent an effective permeability for melt transport that may be channelised into high-porosity, high-permeability dunite channels (e.g. Jull et al., 2002; Kelemen et al., 1995). Our K_0 range of 10^{-13}–10^{-11} m^2 encompasses a change in the amplitude of $\mathcal{G}_{CO_2}$ variation by a factor of 5, a difference in lag of 200 kyrs, and qualitative difference in the time-series of $\mathcal{G}_{CO_2}$ (Fig. 10). Therefore K_0 represents a leading source of uncertainty in the model. Uranium series disequilibria may provide an independent constraint on magma travel time from the base of the melting region (*e.g.*, Jull et al., 2002), although interpreting the various species in the decay chain is fraught with complexity. Preservation of ^{230}Th disequilibrium (half-life of 75 kyrs) suggests a permeability of $K_0 \geq 10^{-12}$ m^2, and community consensus similarly favours K_0 at the higher end of our considered range.

Our model is based on the assumption that melt travels vertically from the depth of first melting to the top of the melting region and is then focused along a sloping, high porosity decompaction channel to the ridge axis (Sparks and Parmentier, 1991). The travel time of the vertical flow is modelled by a 1D compaction column; we assume that transport in the decompaction channel is instantaneous. The systematic error introduced by the latter assumption is zero on the ridge axis ($x = 0$), and increases with distance x from the ridge axis. This means τ plotted in Fig. 4(b) is more accurate at small x, but increasingly underestimates τ for larger x. Therefore, assuming τ_{min} is accurately modelled, τ_{max} is probably too small, such that E_{CO_2} in Fig. 3 should have a longer tail on the right of the graph. However, long tails have little effect on the resultant E_{CO_2} pattern for complex sea-level changes or on the $\mathcal{G}_{CO_2}$ pattern for reconstructed sea level. Therefore the overall effect of including a finite travel time along the high porosity channel would be to make a small adjustment to the E_{CO_2} response. This suggests that assuming instantaneous travel time along the channel has little effect on the results of the model.

Another assumption made is that travel time is constant with respect to time, despite changes in melting rate (and thus, porosity) caused by changing sea-level. This follows the approach in the reduced model of Crowley et al. (2015), where the perturbations in porosity were taken as negligible disturbances to the travel time in a steady-state compaction column solution from Hewitt (2010).

A more significant assumption underpinning the model is that carbon dioxide behaves as a perfectly incompatible tracer — meaning that carbon concentration does not affect the mantle's physical or thermodynamic properties. However, carbon is not a trace element. In contrast, experiments by Kono et al. (2014) document the very low viscosity of incipient, carbon-rich melts present at small melt fraction below the base of the silicate melting region. The experiments also show that viscosity rises sharply as the carbon is diluted by silicate melting. It would be challenging to capture this
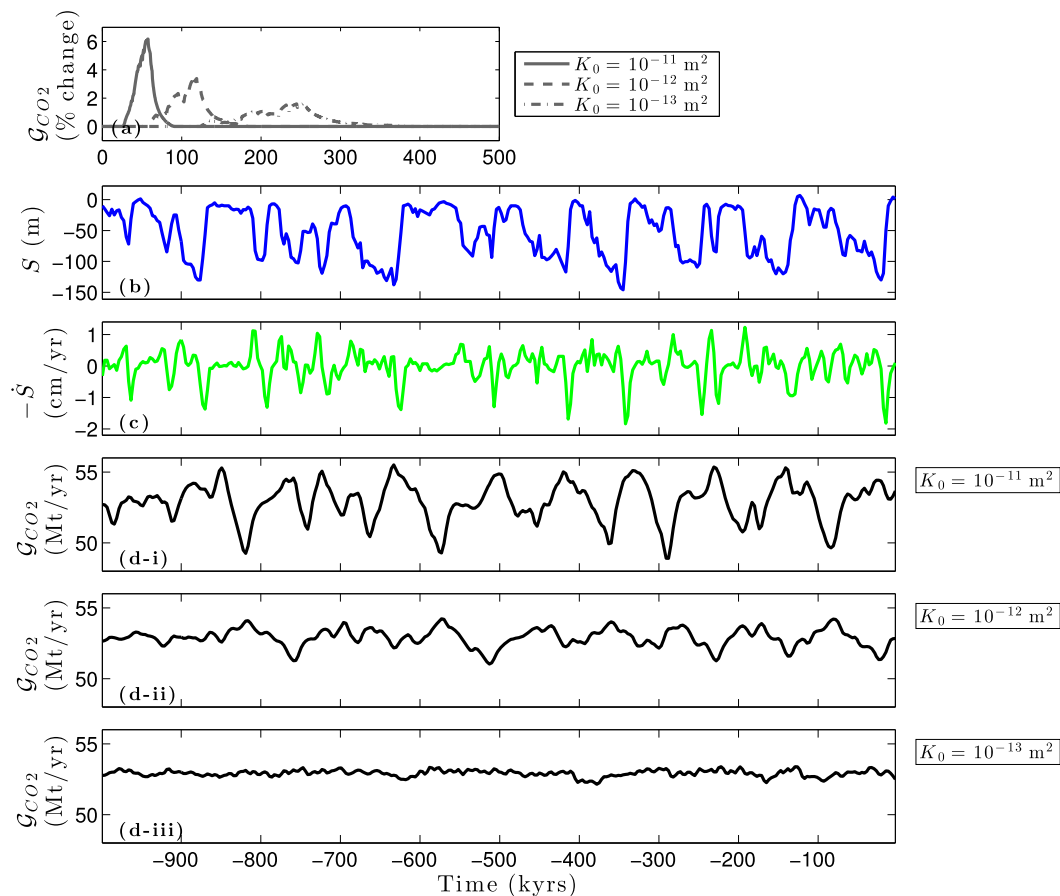
Fig. 10. Global MOR emissions. Panel **(a)** shows CO_2 emissions from the global MOR system for a step change in sea-level identical to that of Fig. 3(a). Subsequent panels consider reconstructed sea level and its effect. **(b)** Reconstructed sea level; **(c)** the negative rate of sea-level change; and **(d–i–iii)** CO_2 emissions from the global MOR system. The sea level time-series has been applied further back in time than shown, such that the left-most point in $\mathcal{G}_{CO_2}$ is affected by more than τ_{max} kyrs of prior sea-level change. For (d-i, ii, iii) the lags in $\mathcal{G}_{CO_2}$ are, respectively, $\sim$60 kyrs, $\sim$120 kyrs, and $\sim$250 kyrs.

variability in models, especially since the wetting properties (and hence the mobility) of carbon-rich melts are poorly constrained.

A more significant concern, however, is that treating volatiles as trace elements neglects their thermodynamic effect on melting. Small mantle concentrations of carbon affect the depth at which melting begins, though the melt fractions produced by this incipient melting are probably less than a few tenths of a percent (Dasgupta et al., 2013). Our model assumes that these melts do not segregate until the onset of silicate melting. At such small porosity, it is unclear whether these carbonated melts can percolate. However, water-induced melting at the wet peridotite solidus of $\sim$90–120 km (Asimow and Langmuir, 2003; Dasgupta et al., 2013) increases the melt fraction. Again, the threshold of interconnectivity for such melts is not known, so it is possible that such deep, hydrous melts do not segregate, or do so very slowly. If the [230]Th disequilibrium observed in young MOR lavas originates with melt segregation in the presence of garnet (Stracke et al., 2006), it would support the hypothesis of efficient segregation of hydrous melts (although other hypotheses also fit the observations). Overall, our model depends only on the presence of a pressure-dependent boundary that separates non-segregating melts, below, from segregating melts, above. The sharpness that is required of this boundary is unclear.

Finally, our model assumes a chemically and thermally homogeneous mantle, which is certainly not true of the natural system (*e.g.*, Dalton et al., 2014). No data exists that would allow us to accurately incorporate small-scale ($\lesssim$100 km) heterogeneity in model. If such heterogeneity is pervasive and at scales of $\sim$10 km or smaller, it would affect the style of melt transport (Katz

and Weatherley, 2012), with fertile regions creating pathways for rapid melt transport through the melting region. It may be the case that this is captured by a high effective permeability, though this is probably not a testable hypothesis. Large-scale heterogeneity would leave the mantle homogeneous over the scale at which we calculate E_{CO_2}, so the underlying melt transport model would be unaffected, though parameters would need to be adjusted according to the oceanic region. It seems likely that such variations would cancel in the integral for global CO_2 emissions rate.

Previous authors have suggested that changing sea level might affect MOR CO_2 emissions almost instantaneously (Huybers and Langmuir, 2009; Lund and Asimow, 2011; Tolstoy, 2015). Their assumption is that pressure changes instantaneously affect melting rates, MOR volcanic productivity and therefore, assuming constant CO_2 concentration in the erupted melt, MOR CO_2 emissions. We disagree with the assumption that CO_2 concentrations would be constant. CO_2 is highly incompatible and therefore additional melting acts to dilute the constant mass of CO_2 in the melt. However, after including these effects, our model can calculate whether changing sea level affects MOR CO_2 emissions (see Appendix A.4). To leading order there is no effect; the reduced (or increased) concentration of CO_2 in the melt counteracts the increased (or reduced) rate of melt delivery to the ridge axis.

We would like to be able to compare the model to data, but there is no dataset of global MOR CO_2 flux over time. Atmospheric CO_2 concentration from Antarctic ice cores (Bereiter et al., 2015) is an existing dataset that might record some influence of $\mathcal{G}_{CO_2}$. However, there are many strong, nonlinear controls on atmospheric CO_2 and the relationship between $\mathcal{G}_{CO_2}$ and atmospheric CO_2 will not

necessarily be constant over time. Nonetheless, comparing atmospheric CO_2 to $\mathcal{G}_{CO_2}$ does offer at least one useful insight: if there is no correlation between these quantities within the model's reasonable parameter space, it would be an indication that MOR CO_2 emissions have no effect on atmospheric CO_2. We find a correlation in Appendix A.5. The best correlation, without considering the very significant complicating factors associated with climatic feedbacks, occurs at $K_0 = 10^{-11.37}$ with a lag of 73 kyrs. This correlation does not prove any causative link between $\mathcal{G}_{CO_2}$ and atmospheric CO_2.

Variable MOR CO_2 emissions' effect on atmospheric CO_2 will vary over time, as the fraction of MOR CO_2 emissions into the intermediate ocean that reach the atmosphere is not constant. This fraction depends upon an array of factors that affect ocean alkalinity, ocean upwelling patterns and CO_2 concentration in the atmosphere, and these factors vary on sub-glacial/glacial timescales (as do numerous processes interacting with them, *e.g.,* the biosphere) (Broecker, 1982; Walker, 1986; Brovkin et al., 2012; Yu et al., 2014). This would have to be taken into account if inferring any climate implications from our model.

The MOR carbon flux may vary over time in other ways that we have not considered here. For instance, it is plausible that the intensity of hydrothermal circulation varies with sea level, driven by variations in melt supply (Lund and Asimow, 2011; Crowley et al., 2015). If this is the case, hydrothermal variations would have a different lag than that of CO_2 emissions. Hydrothermal systems have been proposed as both a CO_2 sink, with hot seawater transforming basalts to clay (Gysi and Stefansson, 2012), and a CO_2 source, with hydrothermal fluids transporting CO_2 from magma to the ocean (Sakai et al., 1990). The rate of both these processes might scale with hydrothermal circulation, although it is not clear whether the net effect would be to increase or decrease MOR CO_2 emissions.

5. Summary

The model presented above builds on the reduced model of Crowley et al. (2015) to calculate the efflux of a highly incompatible chemical component from a mid-ocean ridge, and how that efflux would vary with changes in sea level. It is based on a description of melt transport through a homogeneous mantle and assumes perfect incompatibility of the component. This leads to a simple but physically consistent model of chemical transport through the melting region beneath a ridge. The model calculates total melt supply rate and global background emissions of CO_2 that are consistent with data and prior estimates.

In the model, changing sea level affects the depth of first silicate melting; this alters the rate at which CO_2 enters the melting region, segregates from its mantle source, and (some time later) arrives at the ridge axis and is degassed into the ocean.

The MOR emission rate of CO_2 is predicted to vary by up to 12.5% when the model is forced with reconstructed Pleistocene sea level variation (7 MtCO_2/yr for 125 ppmw $\mathcal{C}_{CO_2}$; 11 MtCO_2/yr for 215 ppmw $\mathcal{C}_{CO_2}$). There is uncertainty in the predicted magnitude and timing (relative to sea-level forcing) of this effect, as two parameters of the model — $\mathcal{C}_{CO_2}$ and K_0 — are weakly constrained by existing data. However, within reasonable ranges of the model parameters, the amplitude of global MOR CO_2 emission-rate variation will remain on the order of several MtCO_2/yr. The total difference in the mass of CO_2 emitted from MORs during sea-level driven deviations from global baseline CO_2 is up to ~80 Gt CO_2 for high permeability and 125 ppmw $\mathcal{C}_{CO_2}$ (see Fig. 10(d-i)). This is 4% of the pre-industrial CO_2 mass in the atmosphere of 2190 Gt, or 0.06% of pre-industrial CO_2 in the oceans (IPCC: Solomon et al., 2007, Fig. 7.3).

Our results indicate that the CO_2 emissions from mid-ocean ridges are temporally variable in response to sea-level change.

These results align with the hypothesis of Huybers and Langmuir (2009); however, whereas they assumed an immediate emissions response, we show that the mid-ocean ridge CO_2 emissions response lags the sea-level forcing by approximately the minimum travel time of CO_2 through the melting region — at least 60 kyrs. Therefore MOR CO_2 emissions cannot feed back into the sea-level change that caused them; instead these CO_2 emissions will enter the climate system during the next glacial cycle. Further work is needed to assess the climatic impact of the variable CO_2 emissions predicted for mid-ocean ridges in this paper and for subaerial volcanoes by Huybers and Langmuir (2009).

Appendix A. Supplementary material

Supplementary material related to this article can be found online at http://dx.doi.org/10.1016/j.epsl.2015.06.031.

References

Asimow, P., Langmuir, C., 2003. The importance of water to oceanic mantle melting regimes. Nature 421 (6925), 815–820. http://dx.doi.org/10.1038/nature01429.

Batchelor, G., 1967. An Introduction to Fluid Mechanics. Cambridge University Press.

Bereiter, B., Eggleston, S., Schmitt, J., Nehrbass-Ahles, C., Stocker, T.F., Fischer, H., Kipfstuhl, S., Chappellaz, J., 2015. Revision of the EPICA Dome C CO_2 record from 800 to 600 kyr before present. Geophys. Res. Lett. 42 (2), 542–549.

Bown, J.W., White, R.S., 1994. Variation with spreading rate of oceanic crustal thickness and geochemistry. Earth Planet. Sci. Lett. 121 (3–4), 435–449.

Broecker, W.S., 1982. Glacial to interglacial changes in ocean chemistry. Prog. Oceanogr. 11 (2), 151–197.

Brovkin, V., Ganopolski, A., Archer, D., Munhoven, G., 2012. Glacial CO_2 cycle as a succession of key physical and biogeochemical processes. Clim. Past 8 (1), 251–264.

Budyko, M.I., Ronov, A.B., Yanshin, A.L., 1987. History of the Earth's Atmosphere. Springer, Berlin, Heidelberg.

Cartigny, P., Pineau, F., Aubaud, C., Javoy, M., 2008. Towards a consistent mantle carbon flux estimate: insights from volatile systematics (H_2O/Ce, delta D, CO_2/Nb) in the North Atlantic mantle (14 degrees N and 34 degrees N). Earth Planet. Sci. Lett. 265 (3–4), 672–685.

Coltice, N., Simon, L., Lecuyer, C., 2004. Carbon isotope cycle and mantle structure. Geophys. Res. Lett. 31 (5).

Connolly, J.A.D., Schmidt, M.W., Solferino, G., Bagdassarov, N., 2009. Permeability of asthenospheric mantle and melt extraction rates at mid-ocean ridges. Nature 462 (7270), 209–212.

Crowley, J.W., Katz, R.F., Huybers, P., Langmuir, C.H., Park, S.H., 2015. Glacial cycles drive variations in the production of oceanic crust. Science. http://dx.doi.org/10.1126/science.1261508.

Dalton, C.A., Langmuir, C.H., Gale, A., 2014. Geophysical and geochemical evidence for deep temperature variations beneath mid-ocean ridges. Science 344. http://dx.doi.org/10.1126/science.1249466.

Dasgupta, R., 2013. Ingassing, storage, and outgassing of terrestrial carbon through geologic time. Rev. Mineral. Geochem. 75 (1), 183–229.

Dasgupta, R., Hirschmann, M.M., 2010. The deep carbon cycle and melting in Earth's interior. Earth Planet. Sci. Lett. 298 (1–2), 1–13.

Dasgupta, R., Mallik, A., Tsuno, K., Withers, A.C., Hirth, G., Hirschmann, M.M., 2013. Carbon-dioxide-rich silicate melt in the Earth's upper mantle. Nature 493 (7431), 211–215.

Gale, A., Dalton, C.A., Langmuir, C.H., Su, Y., Schilling, J.G., 2013. The mean composition of ocean ridge basalts. Geochem. Geophys. Geosyst. 14 (3), 489–518.

Gardeweg, M.C., Sparks, R.S.J., Matthews, S.J., 1998. Evolution of Lascar Volcano, Northern Chile. J. Geol. Soc. 155 (1), 89–104.

Gysi, A.P., Stefansson, A., 2012. Experiments and geochemical modeling of CO_2 sequestration during hydrothermal basalt alteration. Chem. Geol. 306, 10–28.

Hewitt, I.J., 2010. Modelling melting rates in upwelling mantle. Earth Planet. Sci. Lett. 300 (3–4), 264–274.

Huybers, P., Langmuir, C., 2009. Feedback between deglaciation, volcanism, and atmospheric CO_2. Earth Planet. Sci. Lett. 286 (3–4), 479–491.

Jellinek, A.M., Manga, M., Saar, M.O., 2004. Did melting glaciers cause volcanic eruptions in eastern California? Probing the mechanics of dike formation. J. Geophys. Res., Solid Earth 109 (B9).

Jull, M., McKenzie, D., 1996. The effect of deglaciation on mantle melting beneath Iceland. J. Geophys. Res., Planets (1991–2012) 101 (B10), 21815–21828.

Jull, M., Kelemen, P.B., Sims, K., 2002. Consequences of diffuse and channelled porous melt migration on uranium series disequilibria. Geochim. Cosmochim. Acta 66 (23), 4133–4148.

Katz, R.F., 2008. Magma dynamics with the enthalpy method: benchmark solutions and magmatic focusing at mid-ocean ridges. J. Petrol. 49 (12), 2099–2121.

Katz, R.F., Weatherley, S.M., 2012. Consequences of mantle heterogeneity for melt extraction at mid-ocean ridges. Earth Planet. Sci. Lett. 335–336, 226–237. http://dx.doi.org/10.1016/j.epsl.2012.04.042.

Kelemen, P.B., Shimizu, N., Salters, V.J.M., 1995. Extraction of mid-ocean-ridge basalt from the upwelling mantle by focused flow of melt in dunite channels. Earth Planet. Sci. Lett. 375 (6534), 747–753. http://dx.doi.org/10.1038/375747a0. Published online: 29 June 1995.

Kono, Y., Kenney-Benson, C., Hummer, D., Ohfuji, H., Park, C., Shen, G., Wang, Y., Kavner, A., Manning, C.E., 2014. Ultralow viscosity of carbonate melts at high pressures. Nat. Commun. 5, 5091.

Lund, D.C., Asimow, P.D., 2011. Does sea level influence mid-ocean ridge magmatism on Milankovitch timescales? Geochem. Geophys. Geosyst. 12 (12).

Maclennan, J., Jull, M., McKenzie, D., Slater, L., Grönvold, K., 2002. The link between volcanism and deglaciation in Iceland. Geochem. Geophys. Geosyst. 3 (11), 1–25.

Marty, B., Tolstikhin, I.N., 1998. CO2 fluxes from mid-ocean ridges, arcs and plumes. Chem. Geol. 145 (3–4), 233–248.

Miller, K.J., Zhu, W.-l., Montesi, L.G.J., Gaetani, G.A., 2014. Experimental quantification of permeability of partially molten mantle rock. Earth Planet. Sci. Lett. 388, 273–282.

Minarik, W.G., Watson, E.B., 1995. Interconnectivity of carbonate melt at low melt fraction. Earth Planet. Sci. Lett. 133 (3–4), 423–437.

Ribe, N.M., 1985. The deformation and compaction of partial molten zones. Geophys. J. Int. 83 (2), 487–501.

Saal, A.E., Hauri, E.H., Langmuir, C.H., Perfit, M.R., 2002. Vapour undersaturation in primitive mid-ocean-ridge basalt and the volatile content of Earth's upper mantle. Nature 419 (6906), 451–455.

Sakai, H., Gamo, T., Kim, E.S., Tsutsumi, M., Tanaka, T., Ishibashi, J., Wakita, H., Yamano, M., Oomori, T., 1990. Venting of carbon dioxide-rich fluid and hydrate formation in mid-Okinawa trough backarc basin. Science 248 (4959), 1093–1096.

Salters, V., Stracke, A., 2004. Composition of the depleted mantle. Geochem. Geophys. Geosyst. 5 (5).

Siddall, M., Hoenisch, B., Waelbroeck, C., Huybers, P., 2010. Changes in deep Pacific temperature during the mid-Pleistocene transition and Quaternary. Quat. Sci. Rev. http://dx.doi.org/10.1016/j.quascirev.2009.05.011.

Sigvaldason, G.E., Annertz, K., Nilsson, M., 1992. Effect of glacier loading/deloading on volcanism: postglacial volcanic production rate of the Dyngjufjöll area, central Iceland. Bull. Volcanol. 54 (5), 385–392.

Solomon, S., Qin, D., Manning, M., Chen, Z., Marquis, M., Averyt, K., Tignor, M., Miller, H. 2007. Ipcc, 2007: climate change 2007: the physical science basis. Contribution of Working Group I to the fourth assessment report of the Intergovernmental Panel on Climate Change.

Sparks, D.W., Parmentier, E.M., 1991. Melt extraction from the Mantle Beneath spreading centers. Earth Planet. Sci. Lett. 105 (4), 368–377.

Spiegelman, M., McKenzie, D., 1987. Simple 2-D models for melt extraction at mid-ocean ridges and island arcs. Earth Planet. Sci. Lett. 83, 137–152.

Stracke, A., Bourdon, B., McKenzie, D., 2006. Melt extraction in the Earth's mantle: constraints from U–Th–Pa–Ra studies in oceanic basalts. Earth Planet. Sci. Lett. 244, 97–112. http://dx.doi.org/10.1016/j.epsl.2006.01.057.

Tolstoy, M., 2015. Mid-ocean ridge eruptions as a climate valve. Geophys. Res. Lett. 42 (5), 1346–1351.

Turcotte, D.L., Schubert, G., 2002. Geodynamics, 2nd edition. Cambridge University Press.

Turner, A., Katz, R.F., Behn, M.D., 2015. Grain-size dynamics beneath mid-ocean ridges: implications for permeability and melt extraction. Geochem. Geophys. Geosyst. 16, 925–946. http://dx.doi.org/10.1029/2014GC005692.

Tushingham, A.M., Peltier, W.R., 1991. Ice-3G: a new global model of Late Pleistocene deglaciation based upon geophysical predictions of post-glacial relative sea level change. J. Geophys. Res., Planets 96 (B3), 4497–4523.

Walker, J., 1986. Global geochemical cycles of carbon, sulfur and oxygen. Mar. Geol. 70 (1–2), 159–174.

White, R.S., McKenzie, D., Onions, R.K., 1992. Oceanic crustal thickness from seismic measurements and rare-Earth element inversions. J. Geophys. Res., Solid Earth 97 (B13), 19683–19715.

Yu, J., Anderson, R.F., Rohling, E.J., 2014. Deep ocean carbonate chemistry and glacial–interglacial atmospheric CO_2 changes. Oceanography 27 (1), 16–25.